Intraseasonal Variability of the Winter Western Boundary Current in the South China Sea Using Satellite Data and Mooring Observations

Kewei Lyu, Xiao-Yi Yang, Quanan Zheng, Dongxiao Wang, and Jianyu Hu

Abstract—The intraseasonal variability of the winter western boundary current (WBC) in the South China Sea (SCS) is investigated using satellite data and mooring observations. The intraseasonal intensification of the northeasterly wind enhances the cross-shelf sea-level gradient, and, thus, causes the basin-scale cyclonic circulation to spin up within around one week. The Southern Cyclonic Gyre in the southwestern SCS further strengthens due to the intensified inertial recirculation of the WBC. Complex empirical orthogonal function analysis reveals that the large sea-level fluctuation around the downstream WBC can mainly be explained by two dominant modes. The first mode is related to intraseasonal variations of the wind field and its spatial field represents the response of the WBC to the westward Rossby waves originated from the interior basin, while the second mode reflects the southward propagation of mesoscale signals along the WBC. Mooring observations recorded the accelerations of the southward WBC three times in winter 2004/2005. While the first two could be linked to the wind intensification, the third one was associated with a cyclonic eddy closely next to the WBC. Initially, this eddy propagated from the Luzon Strait, where active mesoscale processes associated with the Kuroshio intrusion act as important disturbance sources for the SCS.

Index Terms—Intraseasonal variability (ISV), mesoscale eddy, South China Sea (SCS), western boundary current (WBC).

I. INTRODUCTION

THE South China Sea (SCS), a semienclosed marginal sea of the western Pacific, is featured by pronounced monsoon-oriented seasonal variability. The monsoon wind is an important factor for the formation, maintenance, and seasonal variation of the SCS surface ocean circulation. Meanwhile, the northern SCS circulation is greatly influenced by the Kuroshio intrusion and the nonlinear Rossby waves through the Luzon Strait [1]–[3]. In summer, the SCS ocean circulation is dominated by an anticyclonic gyre in the southern SCS and a cyclonic gyre to the

K. Lyu, X.-Y. Yang, and J. Hu are with the State Key Laboratory of Marine Environmental Science, College of Ocean and Earth Sciences, Xiamen University, Xiamen 361102, China (e-mail: kewei.marine@gmail.com; xyyang@xmu.edu.cn; hujy@xmu.edu.cn).

Q. Zheng is with the Department of Atmospheric and Oceanic Science, University of Maryland, College Park, MD 20742, USA (e-mail: quanan@atmos.umd.edu).

D. Wang is with the State Key Laboratory of Tropical Oceanography, South China Sea Institute of Oceanology, Chinese Academy of Sciences, Guangzhou 510301, China (e-mail: dxwang@scsio.ac.cn).

north. In winter, as driven by the intense northeasterly winds, the whole circulation pattern turns into a cyclonic gyre in the deep basin characterized by energetic western boundary current (WBC). The WBC contributes significantly to redistribute water properties, momentum, energy, and nutrients in the SCS [4]. Embedded in the basin-scale circulation are numerous mesoscale eddies and the wind forcing could be an important generation mechanism [5].

The ocean general circulation in the SCS is more variable than that in the open oceans because of the relatively smaller spatial scale and the multiscale variability of monsoon [4]. Except for the widely reported seasonal and interannual variability [6], [7], the SCS circulation also experiences considerable intraseasonal variability (ISV). Liu *et al.* [8] noticed evident ISV of the SCS thermocline based on ocean temperature observations from three buoys. Zhuang *et al.* [9] analyzed characteristics and origins of the sea surface height (SSH) ISV in the SCS and emphasized the importance of dynamical instabilities for the SSH ISV in the deep basin. Wu *et al.* [10] and Wu and Hsin [11] suggested that the circulation patterns off the southwest Taiwan Island and the strength of Kuroshio intrusion could be modulated by the ISV of the local wind. The Pacific-origin intraseasonal sea-level signals could also propagate into the eastern SCS along the coast of the Philippine Archipelago in the form of coastal trapped waves [12]. In addition, analyses on the sea surface temperature [13] and latent heat flux [14] indicate the significant ISV of the air–sea interaction in the SCS.

There have been studies pointing out that the SCS exhibits remarkable response to the ISV of Asian summer monsoon [15], [16]. They suggested that in response to the intraseasonal wind intensification, the SCS summer double gyre ocean circulation strengthens via Rossby wave adjustment. However, little has been known about the ISV of the SCS winter ocean circulation and its connection to the winter monsoon, especially considering that the SCS exhibits distinct seasonal contrast in both wind regime and background ocean circulation. Using satellite data and mooring observations, this study aims to clarify features and mechanisms for the ISV of the SCS winter ocean circulation, with special focus on the strong WBC. The relevant atmospheric and oceanic processes as well as their different behaviors and roles will be distinguished.

In this paper, Section II describes data and methodology. In Section III, we examine spatial patterns accompanying with the northeasterly wind intensification. Next, we identify propagation features of the SSH ISV in the southwestern SCS in

This article has been accepted for inclusion in a future issue of this journal. Content is final as presented, with the exception of pagination.

2   IEEE JOURNAL OF SELECTED TOPICS IN APPLIED EARTH OBSERVATIONS AND REMOTE SENSING
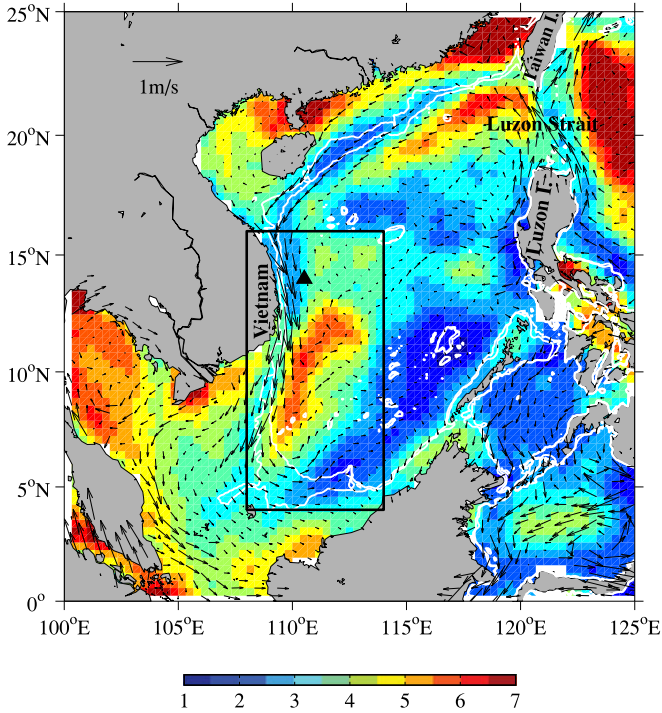

Fig. 1. Multiyear mean surface geostrophic currents (vectors) and standard deviation of 30–90 day filtered SSH (cm, color shading) for October–March during 1999–2009. The white lines show the 100- and 200-m isobaths. The black box denotes the area where the CEOF method is applied for the intraseasonal SSH in Section IV. The black triangle in the western SCS marks the ADCP mooring position.

Section IV. In Section V, mooring observations and case studies in winter 2004/2005 are used to verify possible processes responsible for the ISV of the WBC. Both statistical analysis and dynamical interpretation are applied in this study.

II. DATA AND METHODOLOGY

A. Data

QuikSCAT (Quick Scatterometer) ocean surface vector wind data on a 0.25° by 0.25° grid are obtained from the remote sensing systems (http://www.remss.com). The merged altimeter-based products, including absolute dynamic topography (ADT) and geostrophic current on a 1/3° Mercator grid, are provided by the archiving, validation, and interpretation of satellite oceanographic data (AVISO, http://www.aviso.oceanobs.com). ADT represents the sum of a mean dynamic topography and the time-varying SSH anomaly. Satellite data with a weekly interval from July 1999 to November 2009 are used. Linear spatial and temporal interpolations were used to fill the data gaps.

Over the period from May 2004 to September 2005, an upward-looking acoustic doppler current profiler (ADCP) mooring was deployed at 110°31′E, 13°59′N in the western SCS (see Fig. 1). The ADCP was moored at a depth of 500 m. The vertical bin size of the ADCP data is 8 m. The temporal sampling interval is 30 min before September 2004 and 1 h afterward. The zonal and meridional components of ocean currents were derived from velocity magnitudes and directions recorded by the

ADCP. A 48-h low-pass filter was applied to remove the high-frequency signal in the ADCP raw data. Then, the data were converted into weekly average for direct comparison with the satellite data. The depth range of effective ADCP measurements is 48–480 m. The last bin of ADCP data over 48–56 m was removed. Considering that the climatological mixed layer depth in this region is around 80 m [17], we averaged the ADCP data over 56–80 m to show the variability of upper ocean current.

B. Lagged Regression Analysis

The lagged regression analysis is used to describe the temporal evolution of spatial structures. Given a reference time series x_t, when the dependent variable y_t leads x_t by Δt, the linear regression equation can be solved by the least-square fitting: $y_{t+\Delta t} = ax_t + b + \delta_{t+\Delta t}$, where a is the slope or the regression coefficient at a lag of Δt, b is the intercept, and $\delta_{t+\Delta t}$ is the residual. The statistical significance of regressions is assessed using a t-test $t = r\sqrt{N_{\text{edof}}/(1-r^2)}$, in which r is the correlation coefficient between the two time series, and N_{edof} is the effective degree of freedom. N_{edof} is estimated using the method of Bretherton $et\ al.$ [18] $N_{\text{edof}} = N(1-r_1r_2)/(1+r_1r_2)$, where N is the sample size of the data, and r_1 and r_2 are the lag-one autocorrelations for the two time series, respectively.

C. Complex Empirical Orthogonal Function (CEOF) Analysis

The CEOF method is used to identify propagating features of the variability. In the CEOF analysis, the time series X_t of original dataset is first extended into a complex variable Y_t by adding its Hilbert transform $H(X_t)$ as the imaginary component $Y_t = X_t + iH(X_t)$. The imaginary part $H(X_t)$ is the quadrature function of the real part X_t and represents a simple phase shift by a quarter of one period. Then, a covariance matrix could be constructed from this complex variable Y_t and be processed like the standard empirical orthogonal function (EOF) analysis. The eigenvector V_k and principal component α_k of the kth CEOF mode are complex, providing the amplitude and phase information spatially and temporally. The spatial amplitude A_k is given by $A_k = [V_k V_k^*]^{1/2}$, where V_k^* is the complex conjugate of V_k. The spatial phase θ_k is given by $\theta_k = \tan^{-1}[I(V_k)/R(V_k)]$, where $I(V_k)$ and $R(V_k)$ represent the imaginary and real parts of V_k, respectively. The temporal amplitude and phase can be derived from α_k similarly. A time series for each mode is derived from multiplying the temporal amplitude by the cosine of temporal phase. More details about the CEOF method can be found in Hannachi $et\ al.$ [19].

III. BASIN-SCALE CHARACTERISTICS OF THE WINTER WIND AND OCEAN CIRCULATION ISV

In order to extract intraseasonal signals, a 30–90 day Lanczos bandpass filter was applied to the data. Such period band is commonly used in ISV studies (e.g., [13], [14]). Then, only the boreal winter data were retained in the following analysis. Here, the winter is extended from October to the following March, when the SCS is mainly controlled by the winter monsoon. The

anomaly mentioned below always refers to the bandpass filtered (i.e., intraseasonal) anomaly.

A. Winter-Mean Circulation and Variance Analysis

As shown by the winter-mean surface geostrophic currents (see Fig. 1), the winter WBC flows from the northern SCS and runs southwestward along the continental shelf and slope. Upon reaching the central Vietnam coast, it turns southward and becomes stronger and narrower. After separating from the Vietnam coast, the surface geostrophic current continues to flow southward along the continental shelf, following the 100- or 200-m isobath. The southward WBC turns eastward around 5°N, forming an inertial recirculation pattern, which was named the SCS Southern Cyclonic Gyre [20]. Similar cyclonic structure can also be reproduced by the numerical model and explained as the recirculation associated with the separation of southward WBC from the Vietnam coast [2], [21].

The standard deviation of the filtered SSH in winter (see Fig. 1) shows two bands with strong SSH ISV in the deep basin of the SCS [9]. The northern band is located at the southwest of the Taiwan Island, where the large SSH intraseasonal variance corresponds to the high eddy occurrence [22] and the strong dynamical instability [9] associated with the Kuroshio intrusion. The southwestward orientation of this band is due to the southwestward propagation of mesoscale eddies with a speed of about 10 cm·s^{-1} [23], [24], which could be attributed to the steering effects of the bathymetry and the advection of the mean flow [25]. The southern band lies closely in the east of the WBC in the southwestern SCS. This band has been linked to the southward eddy propagation [25] and the barotropic instability [9].

While the basic features of the SCS winter ocean circulation have been described, the following issues still need to be clarified: to what extent the SSH ISV could be linked to the wind ISV and how the SCS winter ocean circulation responses to the northeasterly wind intensification?

B. Ocean Responses to the Intraseasonal Wind Intensification

The winter northeasterly wind in the SCS is characterized by high wind speed and steady wind direction [26]. This means that the scalar wind speed itself, regardless of the direction, can be used to describe the variability of the winter monsoon. An index defined as the area mean of the 30–90 day filtered wind speed over the SCS (10°–25°N, 100°–125°E) is calculated to represent the wind ISV. The wind index exhibits a high consistency with the time series of the winter wind EOF leading mode, with the temporal correlation being close to 1. Regression maps of the filtered wind vector and wind stress curl onto the wind index are shown in Fig. 2. The anomalous northerly winds predominate most of the SCS and show the maximum amplitude over the northern SCS. The wind stress curl anomaly distribution generally exhibits positive values in the deep basin and negative values over the northern continental shelf. Both patterns resemble their winter mean fields (not shown), indicating the enhancement of the mean state.

Lagged regression patterns of the filtered SSH and surface geostrophic currents on the wind index are shown in Fig. 3. At
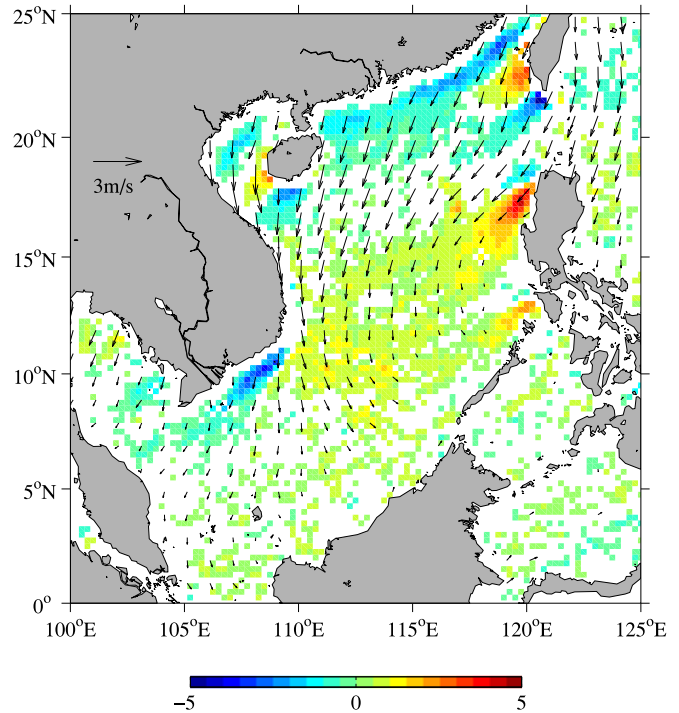

Fig. 2. Regression map of the filtered sea surface wind (vectors) and wind stress curl (10^{-7} N·m^{-3}, color shading) versus the wind index with no lag. Only regions with correlation coefficients >90% significance level are plotted.

lag0 (no lag), accompanying with the northeasterly wind intensification, the large positive SSH anomaly appears in shallow waters around the SCS [see Fig. 3(a)]. The ratio of variance explained by the linear regression, calculated as the square of the maximum correlation coefficient, is generally higher than 60% in shallow waters (not shown). The related ocean dynamics have been suggested to be the direct barotropic wind-driven setup of sea level and the shallow depth acts as an amplifier [27]. The involvement of coastal trapped Kelvin wave is possible [28] but uncertain because its speed is too fast to be distinguished by the weekly averaged data. With the positive SSH anomaly to the right on continental shelves, the anomalous southwestward and southward currents appear along the continental break between the deep basin and shallow waters in the northern SCS and the western boundary region, respectively.

In response to the positive wind stress curl anomaly (see Fig. 2), the negative SSH anomaly occurs in the deep basin one week later at lag1 [see Fig. 3(b)]. The negative SSH anomaly in the deep basin and the positive SSH anomaly in the shallow water jointly enlarge the sea-level gradient across the continental slope, by which the basin-scale cyclonic circulation continues to intensify. The largest velocity anomaly can be found along the western and eastern boundaries of the SCS deep basin. The velocity of the southward WBC increases by up to 15 cm·s^{-1} at ~6°N and 5 cm·s^{-1} at ~14°N [see Fig. 3(b)]. A WBC index is calculated as the filtered mean meridional velocities along the western boundary of the SCS (5°–15°N, 109°–110°E). The wind index leads the WBC index one week with the correlation of −0.65.

This article has been accepted for inclusion in a future issue of this journal. Content is final as presented, with the exception of pagination.

4   IEEE JOURNAL OF SELECTED TOPICS IN APPLIED EARTH OBSERVATIONS AND REMOTE SENSING
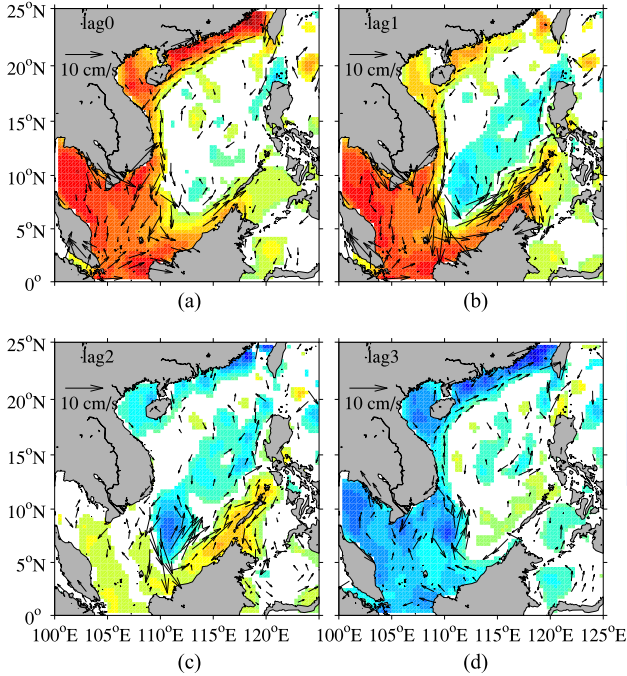

Fig. 3.   Lagged regression maps of the filtered SSH (cm, color shading) and geostrophic currents (vectors) versus the wind index. Only regions with correlation coefficients >90% significance level are plotted.

Fig. 4.   Time-longitude distribution of regressed SSH anomaly (cm) along 8°N onto the wind index.

At lag2 [see Fig. 3(c); two weeks after the wind intensification], a large negative SSH anomaly area with the anomalous cyclonic circulation around is locally formed in the southwestern corner of the SCS deep basin. Besides the southward velocity anomaly along the western boundary, the northward velocity anomaly with the maximum value of 10 cm·s^{-1} also appears along the eastern flank. Spatially, the overlying wind stress curl anomaly (see Fig. 2) is too weak to account for such large anomaly. Also, this eddy-like anomaly area forms after the wind intensification but with a lag of two weeks. Both facts indicate that the local wind forcing could not be the key process. We suggest that such anomaly pattern should be explained as the enhancement of the background Southern Cyclonic Gyre, which is generated through the WBC related inertial recirculation rather than through the local Ekman pumping. This negative anomaly area is located east of 110°E at lag2. By lag3 [see Fig. 3(d)], it slightly migrates westward with the center at around 110°E. However, the zonal shift cannot be easily discerned from the spatial maps. Fig. 4 shows the time-longitude distribution of the SSH anomaly value along 8°N. While the sea level in shallow waters rises or falls with the wind, the westward propagation behavior can be seen in the deep basin east of 108°E. It can be estimated from Fig. 4 that the westward phase speed is about 20–30 cm·s^{-1}, which is consistent with the westward phase speed of the first baroclinic Rossby wave in the southern SCS [29]. This wind-driven process is different from the southward eddy motion discussed by Zhuang *et al.* [9], [25] and has not been analyzed before. Different features of both processes and their relative importance need to be examined. In the next section, by separating these two processes, we will give a detailed inspection into the strong SSH ISV in the southwestern SCS.
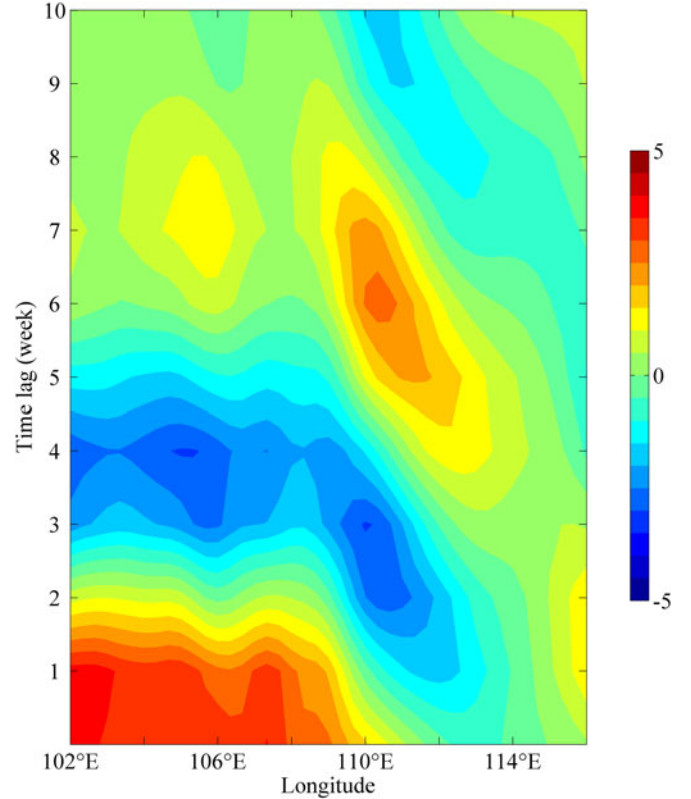
Along a long band stretching from the Luzon Strait to the central Vietnam, there exists no obvious statistical correlation between the wind index and the SSH anomaly throughout the entire process in Fig. 3. First, the wind stress curl does not show significant anomaly over this band (see Fig. 2). Also, as mentioned above, the SSH in this region is mainly modulated by active mesoscale eddies. Note that there exist statistically significant anomaly values around the Luzon Strait. At lag0 [see Fig. 3(a)], the negative anomaly appears in the southern Luzon Strait, while the positive anomaly lies to the northwest. This distribution can be explained by the northwestward Ekman transport due to the intensified northeasterly wind. The negative wind stress curl anomaly south of Taiwan (see Fig. 2) also contributes to the local amplification of the positive SSH anomaly. Such SSH anomaly patterns have been suggested to facilitate the westward intrusion of the Kuroshio [11].

IV. Two Dominant Processes in the Southwestern SCS

Here, the CEOF method is used to identify key processes that govern the strong SSH ISV around the southward WBC. Within a spatial domain 4°–16°N, 108°–114°E as denoted in Fig. 1, the CEOF analysis is applied to the 30–90 day filtered SSH from October to March. Fig. 5 illustrates the variance percentage explained by each CEOF mode, where the error bars are determined based on the criterion developed by North *et al.* [30]. The first two leading modes, which stand out from

This article has been accepted for inclusion in a future issue of this journal. Content is final as presented, with the exception of pagination.

LYU *et al.*: INTRASEASONAL VARIABILITY OF THE WINTER WESTERN BOUNDARY CURRENT IN THE SOUTH CHINA SEA   5
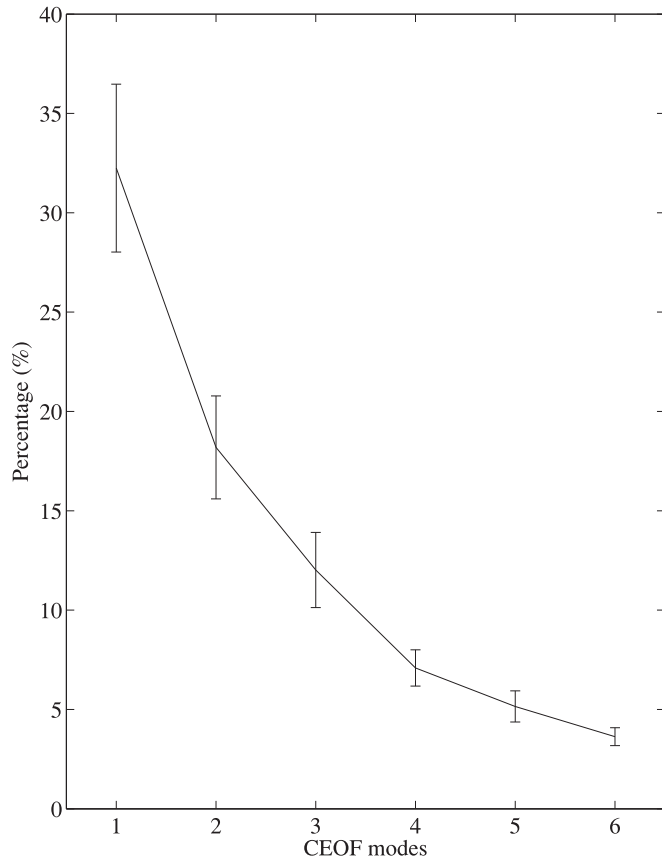

Fig. 5. Percentage of total variance explained by each CEOF mode. Vertical bars represent approximate 95% limits using the formula by North *et al.* [30], in which the effective degree of freedom is determined according to Bretherton *et al.* [18].

remaining modes and are also separated from each other, will be discussed here.

The first mode (CEOF1) contributes about 32.2% of the total variance. The CEOF1 time series [see Fig. 6(a)] is highly correlated with the wind index and the WBC index, with the maximum correlation of 0.64 and 0.79, respectively. Such temporal correlations suggest that the CEOF1 mainly reflects the dynamical response of the southwestern SCS to the intraseasonally varying wind. The spatial amplitude and phase for CEOF1 are shown in Fig. 7(a). The increased spatial phase indicates the propagation direction of the SSH anomaly. It can be seen that the phase values increase evenly from east to west. This feature of westward propagation suggests a possible connection to the Rossby waves. With the typical period of 6–8 weeks according to the time series [see Fig. 6(a)] and the zonal half-wavelength (180° phase difference) of ~5°, the phase speed is about 23–30 cm·s^{-1}, which agrees with that estimated from the time-longitude diagram (see Fig. 4). However, the westward propagation behavior can only be found in the southern SCS. This phenomenon may be interpreted as the restriction of the critical period T_c, which is defined as $T_c = (4\pi f)/(\beta c_1)$, where c_1 is the first baroclinic gravity-wave phase speed, and β is the variation of the Coriolis parameter f with latitude. At given latitude, T_c is the theoretical cut-off period for freely propagating baroclinic Rossby waves. With a typical value of ~2.5 m·s^{-1}

for c_1 at 12°N [29], the calculated T_c is ~78 days. As T_c increases northward, at higher latitudes, the SSH perturbances within intraseasonal timescale can hardly propagate westward in the form of free Rossby waves.

The spatial amplitude represents the intensity of propagating signals and their local manifestation. The large amplitude for CEOF1 is only confined to the west of 112°E between 6° and 11°N [see Fig. 7(a)]. With respect to the largest amplitude near the WBC, we propose two possible mechanisms. First, the SSH anomaly occurred in the interior SCS could propagate westward in the form of Rossby waves. The westward Rossby waves tend to induce the fluctuation of the WBC. Since the SSH distribution around the strong southward WBC is characterized by large zonal gradient and dense isolines, a slight zonal shift of the WBC would lead to large SSH anomaly around its mainstream. Second, the background field becomes more unstable when the winds intensify. The intensified WBC induces larger horizontal shears, allowing barotropic instabilities to develop. The enhanced Southern Cyclonic Gyre means the stronger doming of isopycnals inside it, and, thus, larger zonal density gradient across the WBC. According to the thermal wind relation, this implies larger vertical shears of the southward WBC, which provides a favorable condition for baroclinic instability. Both kinds of instabilities are, thus, capable for generating WBC fluctuations and large SSH anomaly.

The second mode [CEOF2; Fig. 7(b)] accounts for about 18.2% of the total variance. The correlation between its time series [see Fig. 6(b)] and the wind index is statistically insignificant (~0.25). In contrast to the CEOF1, the CEOF2 exhibits its largest amplitude within a small area of 10°–13°N, 109°–112°E. The CEOF2 spatial phase distribution indicates very similar propagating features as mesoscale eddies in the SCS. For example, to the south of the maximum anomaly center, the spatial phase values gradually increase, denoting a southward propagation feature along the WBC. Such southward propagations of the SSH anomaly could be related to southward movements of cyclonic eddies that mainly occur during autumn and winter [25], [31]. The phase difference of 360° between 4°–12°N stands for a full wavelength. For the typical period of 6–8 weeks, according to the time series [see Fig. 6(b)], the calculated southward phase speed is about 18–24 cm·s^{-1}, close to the value of 19 cm·s^{-1} estimated from the direct time-latitude lag correlation [9]. In addition, to the east and north of the maximum anomaly center, the overlying phase values increase toward it, indicating propagating signals from the east and north. Such spatial phase distribution agrees well with the quasi-westward (southwestward) propagation of mesoscale eddies in the central (northern) SCS [31], [32]. Therefore, the CEOF2 could be explained as interactions between the WBC and mesoscale eddies.

Fig. 7(c) shows the variance distribution for the 30–90 day filtered SSH in winter, superimposed with the percentage that can be explained by the first two CEOF modes together. The locally explained variance percentage is relatively lower in the interior ocean (<40%), but increases to the west and peaks at ~80% near the WBC. Over the area with large variance values, CEOF1 and CEOF2 generally explain more than 70% of the local intraseasonal variance. The high percentages presented
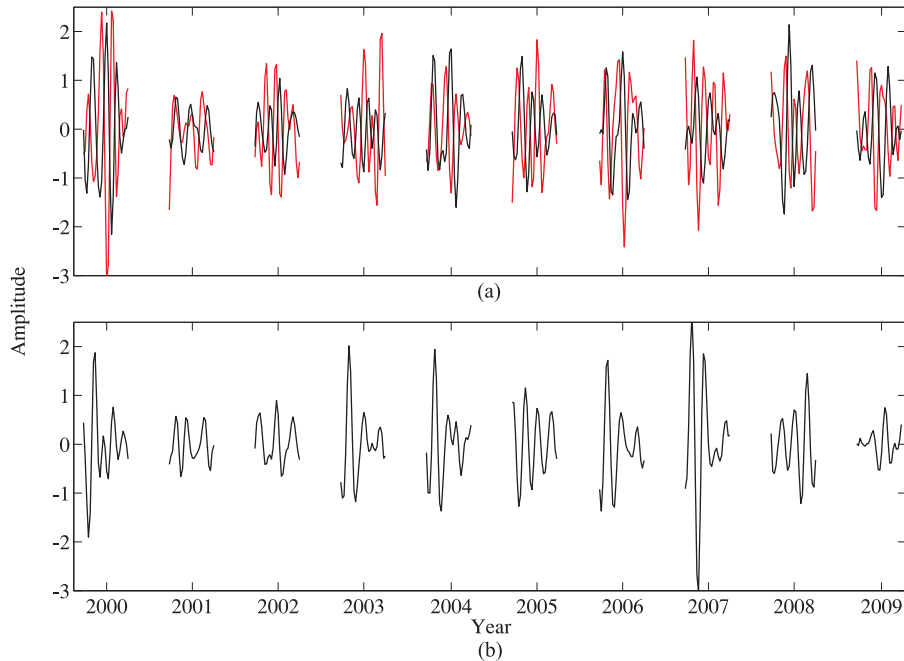
Fig. 6.   Time series for (a) the CEOF1 (black, unitless) together with the wind index (red, m·s^{-1}) and (b) the CEOF2 (black, unitless).
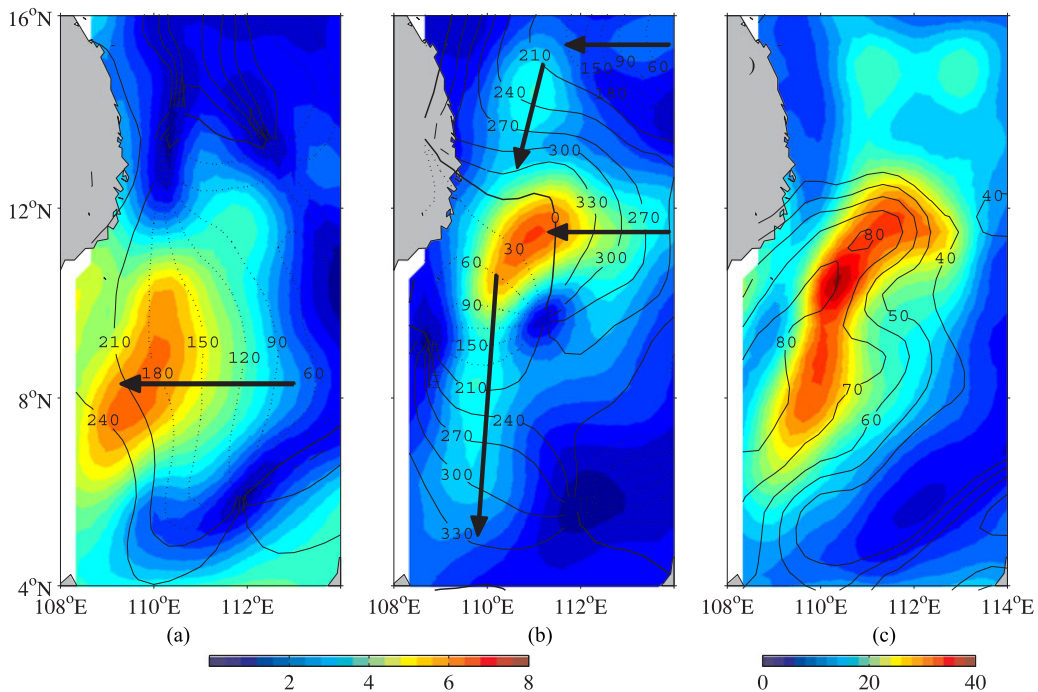

Fig. 7.   Spatial amplitude (color shading, cm) and phase (contours with the interval of 30°) corresponding to the (a) CEOF1 and (b) CEOF2 of the 30–90 day filtered SSH from October to March. Arrows indicate directions of the increased spatial phase, and, thus, the propagating signals. (c) Local variance of the 30–90 day filtered SSH from October to March (color shading, cm^2) and the percentage (contours, %) explained by these two modes.

here provide strong evidence for the local significance of these two CEOF modes in the WBC region. Thus, it can be concluded that the CEOF analysis captures the dominant modes for the strong SSH ISV around the southward WBC. Note that the first two CEOF modes for the meridional component of geographic currents also show very similar propagating features.

It is interesting to note that these two CEOF modes are similar to those identified around the East Australian Current, which is the WBC of the South Pacific subtropical gyre. Using satellite altimeter data and model result, Wilkin and Zhang [33] found that the first two dominant CEOF modes of mesoscale variability in this region are also featured by southwestward
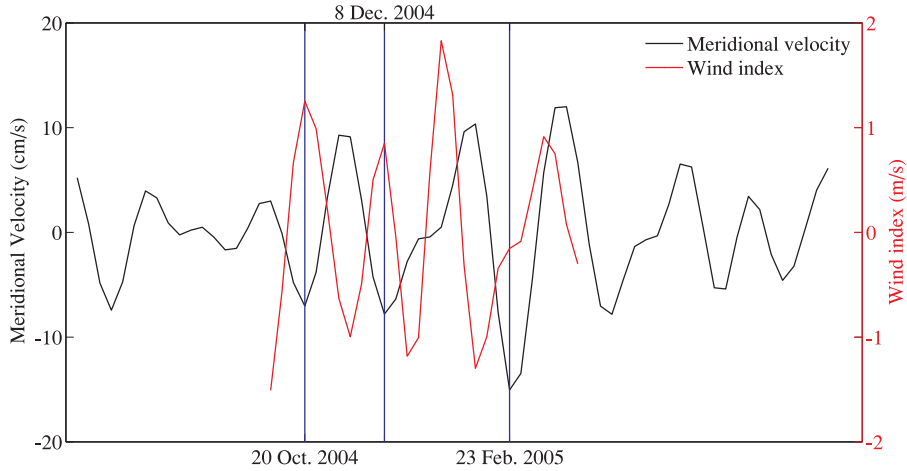
This article has been accepted for inclusion in a future issue of this journal. Content is final as presented, with the exception of pagination.

LYU *et al.*: INTRASEASONAL VARIABILITY OF THE WINTER WESTERN BOUNDARY CURRENT IN THE SOUTH CHINA SEA

7

Fig. 8. Wind index (red line, $m \cdot s^{-1}$) and the 30–90 day bandpass filtered meridional velocity (black line, $cm \cdot s^{-1}$) measured by the ADCP mooring (averaged over 56–80 m). Time series for wind index is shifted forward by one week.
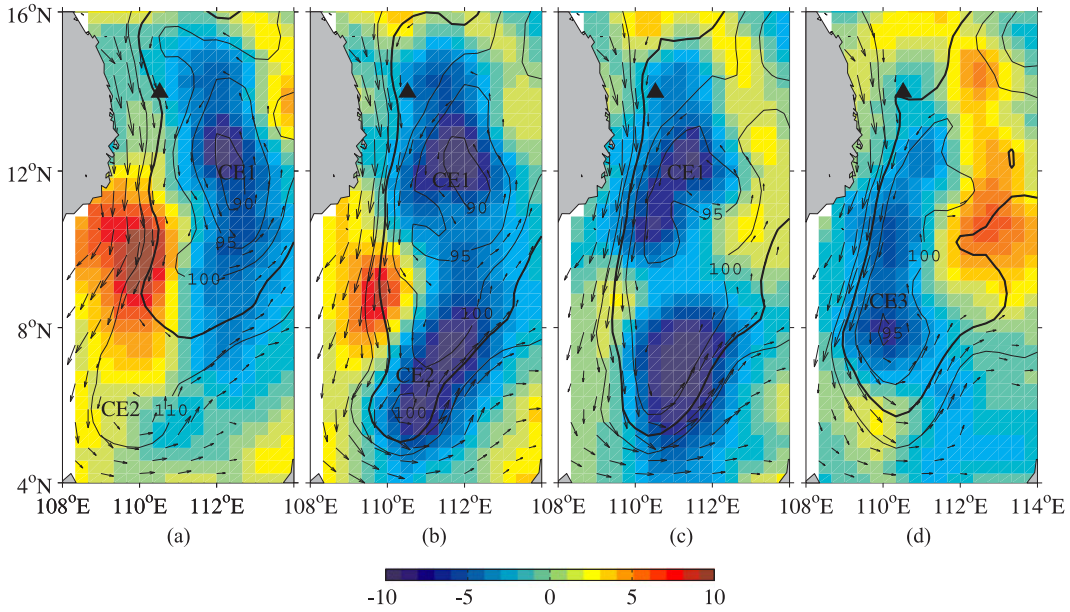

Fig. 9. Weekly averaged maps of ADT (cm, contours with 5-cm interval), geostrophic currents (vectors) greater than 20 $cm \cdot s^{-1}$, and 30–90 day filtered SSH anomaly (cm, color shading) centered on (a) 1, (b) 8, (c) 15, and (d) 22 December, 2004. The 105-cm contours are in bold. The black triangle marks the ADCP mooring position.

propagation along the coast and westward propagation toward the coast, respectively; they referred to these two CEOF modes as eddy mode and wave mode, respectively. This comparison reflects that these two WBC system share similarities not only in the mean filed (i.e., southward boundary current), but also in propagation features of the SSH variability.

V. MOORING OBSERVATIONS AND CASE STUDIES IN WINTER 2004/2005

Time series of the 30–90 day filtered meridional velocities observed by the mooring from May 2004 to September 2005 is shown in Fig. 8. The northeasterly wind index with time lag of one week is also plotted for comparison. Here, we only discuss mooring observations during the winter, while the summer ocean circulation might be influenced by the ISV of Asian summer monsoon [15], [16]. Based on regression maps of the geostrophic current (see Fig. 3), the enhanced southward WBC (negative velocity anomaly) corresponds to the intensified wind. That means if the WBC only varies with the wind ISV, these two time series should be negatively related to each other. On 20 October and 8 December 2004, the mooring measured southward velocity increased by ~7 and ~8 $cm \cdot s^{-1}$, respectively. Such corresponding relationship between the wind and the WBC supports that the southward WBC responds quickly to the wind intensification and speeds up within one week. Fig. 9 represents a typical wind ISV modulated case in the southwestern SCS. Spatial evolution patterns for the ADT, geostrophic currents,

and the filtered SSH anomaly in December 2004 are shown. According to the wind index, four weeks from 1 December to 22 December correspond to lag0 through lag3 of regression maps in Fig. 3. The cyclonic eddies described below were identified visually based on the criteria that there exist closed ADT contours with local minima in the center and cyclonic geostrophic currents around.

On 1 December, 2004 [see Fig. 9(a)], the overall patterns presented a cyclonic circulation structure with a strong WBC. A cyclonic eddy (CE1) with lower central ADT value of 90 cm and negative SSH anomaly existed around (112°E, 12°N). To the southern tip of the southward WBC, there was also a cyclonic eddy (CE2) with much smaller size. One week later on 8 December [see Fig. 9(b)], in response to the intensified wind, low ADT area enclosed by the 100- or 105-cm isoline expanded southward and enlarged. In Fig. 9(c), CE1 weakened and migrated westward. In the southern part, CE2 disappeared while the negative SSH anomaly became larger and the recirculation pattern became clear. Such change implies that the gyre-scale wind-forced dynamics dominated the regional circulation, resulting in the weakening of the embedded mesoscale structure. By 22 December as shown in Fig. 9(d), the area with the ADT value <100 cm and negative SSH anomaly reduced and only existed along the eastern flank of the WBC. Throughout the entire process, the 105-cm isoline (highlighted by the thick line) shifted westward slightly, especially in the lower latitude south of 10°N. This case clearly presents how the southwestern SCS responds to the wind intensification. The spatial-temporal evolution agrees well with our interpretation for the lagged regression maps (see Fig. 3). Also, we note that the life history of CE1 follows the role of CEOF2. As CE1 moved to the west along ~12°N and approached the WBC, the remnant mesoscale signal seemed to propagate southward along the WBC. In Fig. 9(d), one can see that a new cyclonic eddy (CE3) was formed to the south.

On 23 February, 2005, the mooring also recorded that the southward current increased by ~15 cm·s^{-1}, while no intraseasonal wind intensification occurred (see Fig. 8). The satellite altimeter observations show that there was a cyclonic eddy (C2) near the WBC on 23 February [see Fig. 10(b)]. The mooring was located around its western flank and recorded the strong southward current. Along the southwestward eddy propagation band in the northern SCS, this cyclonic eddy can be traced back to the lower ADT area (C1) northwest of the Luzon Island [see Fig. 10(a)], which is known as the Northwest Luzon Cyclonic Gyre [20]. In order to track the movement of this cyclonic eddy from C1 to C2, we first detected the associated low ADT areas from each weekly ADT map, and, then, found their centers with the lowest ADT (red dots). The propagation path is shown as the red lines in Fig. 10 by connecting the red dots. In fact, eddies are frequently generated around the Luzon Strait and move southwestward [32]. Some of them can even travel to the western coast, such as this case captured by *in situ* mooring. The detailed discussion about eddy generation mechanisms around the Luzon Strait is beyond the scope of this paper, while the nonlinear Rossby eddies from the Pacific and the local wind have been proposed to be important drivers [3], [11], [34].
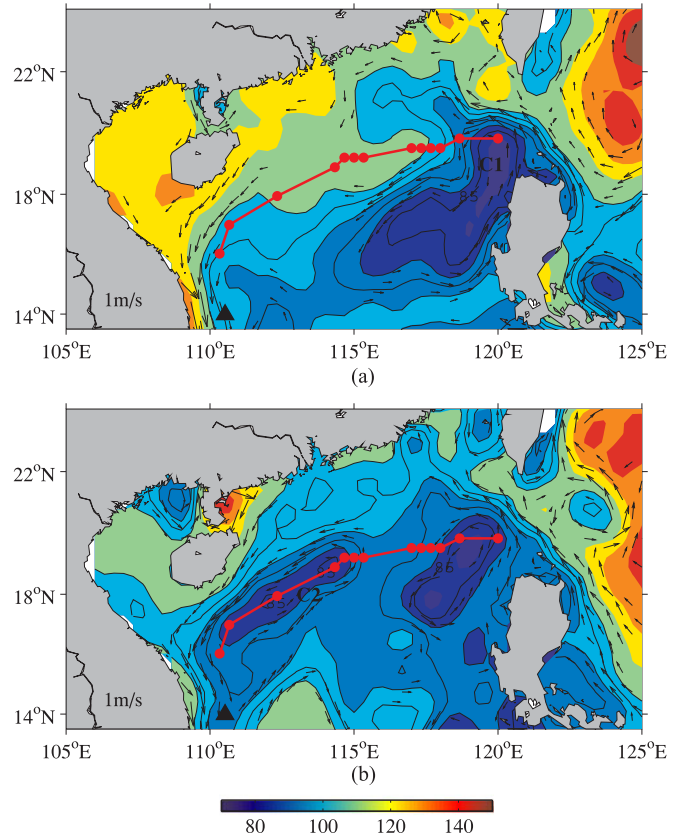

Fig. 10. ADT (color shading superimposed with 85–110-cm contours) and geostrophic currents greater than 20 cm·s^{-1} (vectors) maps in the northern SCS on (a) 1 December, 2004 and (b) 23 February, 2005. The black triangle marks the ADCP mooring position. Red lines show the eddy movements from C1 to C2, by connecting their central points (red dots) on weekly maps.

VI. SUMMARY

Using satellite data comprising of the sea surface wind, SSH and geostrophic current, and ADCP mooring current data in the western SCS during the winter 2004/2005, this paper analyzes features and mechanisms of the winter WBC ISV in the SCS. Dynamical adjustments of the SCS to the wind ISV during winter are summarized into the following four processes: 1) In response to the intraseasonal intensification of northeasterly winds, the SSH rises in shallow waters because of the alongshore wind anomaly but falls in the deep ocean due to the negative wind stress curl anomaly, driving the basin-scale cyclonic circulation to intensify within around one week; 2) around two weeks later, forced by the intensified inertial recirculation associated with the WBC, the Southern Cyclonic Gyre in the southwestern SCS is further enhanced; 3) in the southern SCS, the wind-forced intraseasonal SSH anomaly could propagate westward in the form of Rossby waves; 4) under the impact of incoming westward Rossby waves, the downstream WBC fluctuates and induces the largest SSH anomaly around it. The above processes are supported by evidences from the regression analysis, the first mode of the CEOF analysis, the ADCP mooring observations, and a case study. The understanding of such wind-driven process in winter, together with the work that has been done for the

This article has been accepted for inclusion in a future issue of this journal. Content is final as presented, with the exception of pagination.

LYU *et al.*: INTRASEASONAL VARIABILITY OF THE WINTER WESTERN BOUNDARY CURRENT IN THE SOUTH CHINA SEA

9

summer counterpart [15], [16], may provide useful predictability for short-term variations of the SCS seasonal ocean circulation.

Besides the wind ISV, the ADCP mooring also recorded the enhanced southward WBC associated with a cyclonic eddy, which was originated from the Luzon Strait and propagated southwestward to the western boundary of the SCS. According to the second CEOF mode and case studies, we emphasize that the oceanic mesoscale eddies, either from the upstream WBC or from the interior ocean, tend to move southward along the strong WBC and lead to short-term fluctuations of the WBC. Further research will focus on the detailed mechanism of the interaction between the WBC and mesoscale eddies, as also suggested by Wang *et al.* [35].

REFERENCES

[1] J. Hu, H. Kawamura, H. Hong, and Y. Qi, "A review on the currents in the South China Sea: Seasonal circulation, South China Sea warm current and Kuroshio intrusion," *J. Oceanogr.*, vol. 56, no. 6, pp. 607–624, 2000.

[2] J. Gan, H. Li, E. N. Curchitser, and D. B. Haidvogel, "Modeling South China Sea circulation: Response to seasonal forcing regimes," *J. Geophys. Res.*, vol. 111, 2006, Art. no. C06034.

[3] Q. Zheng, C.-K. Tai, J. Hu, H. Lin, R.-H. Zhang, F.-C. Su, and X. Yang, "Satellite altimeter observations of nonlinear Rossby eddy–Kuroshio interaction at the Luzon Strait," *J. Oceanogr.*, vol. 67, no. 4, pp. 365–376, 2011.

[4] G. Fang, G. Wang, Y. Fang, and W. Fang, "A review on the South China Sea western boundary current," *Acta Ocean. Sin.*, vol. 31, no. 5, pp. 1–10, 2012.

[5] G. Wang, D. Chen, and J. Su, "Winter eddy genesis in the eastern South China Sea due to orographic wind jets," *J. Phys. Oceanogr.*, vol. 38, no. 3, pp. 726–732, 2008.

[6] C.-R. Ho, Q. Zheng, Y. S. Soong, N.-J. Kuo, and J.-H. Hu, "Seasonal variability of sea surface height in the South China Sea observed with TOPEX/Poseidon altimeter data," *J. Geophys. Res.*, vol. 105, no. C6, pp. 13981–13990, 2000.

[7] Q. Liu, X. Jiang, S. Xie, and W. T. Liu, "A gap in the Indo-Pacific warm pool over the South China Sea in boreal winter: Seasonal development and interannual variability," *J. Geophys. Res.*, vol. 109, 2004, Art. no. C07012.

[8] Q. Liu, Y. Jia, P. Liu, Q. Wang, and P. C. Chu, "Seasonal and intraseasonal thermocline variability in the central South China Sea," *Geophys. Res. Lett.*, vol. 28, no. 23, pp. 4467–4470, 2001.

[9] W. Zhuang, S.-P. Xie, D. Wang, B. Taguchi, H. Aiki, and H. Sasaki, "Intraseasonal variability in sea surface height over the South China Sea," *J. Geophys. Res.*, vol. 115, 2010, Art. no. C04010.

[10] C.-R. Wu, T. Y. Tang, and S. F. Lin, "Intra-seasonal variation in the velocity field of the northeastern South China Sea," *Continental Shelf Res.*, vol. 25, no. 17, pp. 2075–2083, 2005.

[11] C.-R. Wu and Y.-C. Hsin, "The forcing mechanism leading to the Kuroshio intrusion into the South China Sea," *J. Geophys. Res.*, vol. 117, 2012, Art. no. C07015.

[12] X. Chen, B. Qiu, X. Cheng, Y. Qi, and Y. Du, "Intra-seasonal variability of Pacific-origin sea level anomalies around the Philippine Archipelago," *J. Oceanogr.*, vol. 71, no. 3, pp. 239–249, 2015.

[13] R. Gao and F. Zhou, "Monsoonal characteristics revealed by intraseasonal variability of sea surface temperature (SST) in the South China Sea (SCS)," *Geophys. Res. Lett.*, vol. 29, no. 8, pp. 63–1—63-4, 2002.

[14] L. Zeng and D. Wang, "Intraseasonal variability of latent-heat flux in the South China Sea," *Theor. Appl. Climatol.*, vol. 97, pp. 53–64, 2009.

[15] S.-P. Xie, C.-H. Chang, Q. Xie, and D. Wang, "Intraseasonal variability in the summer South China Sea: Wind jet, cold filament, and recirculations," *J. Geophys. Res.*, vol. 112, 2007, Art. no. C10008.

[16] G. Wang, Z. Ling, R. Wu, and C. Chen, "Impacts of the Madden–Julian oscillation on the summer South China Sea Ocean circulation and temperature," *J. Climate*, vol. 26, no. 20, pp. 8084–8096, 2013.

[17] X. Wu, Q. Xie, Z. He, and D. Wang, "Free and forced Rossby waves in the western South China Sea inferred from Jason-1 satellite altimetry data," *Sensors*, vol. 8, no. 6, pp. 3633–3642, 2008.

[18] C. S. Bretherton, M. Widmann, V. P. Dymnikov, J. M. Wallace, and I. Bladé, "The effective number of spatial degrees of freedom of a time-varying field," *J. Climate*, vol. 12, no. 7, pp. 1990–2009, 1999.

[19] A. Hannachi, I. T. Jolliffe, and D. B. Stephenson, "Empirical orthogonal functions and related techniques in atmospheric science: A review," *Int. J. Climatol.*, vol. 27, no. 9, pp. 1119–1152, 2007.

[20] G. Fang, W.-d. Fang, Y. Fang, and K. Wang, "A survey of studies on the South China Sea upper ocean circulation," *Acta Oceanographica Taiwanica*, vol. 37, no. 1, pp. 1–16, 1998.

[21] J. Gan and T. Qu, "Coastal jet separation and associated flow variability in the southwest South China Sea," *Deep Sea Res. Part I*, vol. 55, no. 1, pp. 1–19, 2008.

[22] F. Nan, H. Xue, P. Xiu, F. Chai, M. Shi, and P. Guo, "Oceanic eddy formation and propagation southwest of Taiwan," *J. Geophys. Res.*, vol. 116, 2011, Art. no. C12045.

[23] C.-R. Wu and T.-L. Chiang, "Mesoscale eddies in the northern South China Sea," *Deep Sea Res. Part II*, vol. 54, nos. 14/15, pp. 1575–1588, 2007.

[24] D. Wang, H. Xu, J. Lin, and J. Hu, "Anticyclonic eddies in the northeastern South China Sea during winter 2003/2004," *J. Oceanogr.*, vol. 64, no. 6, pp. 925–935, 2008.

[25] W. Zhuang, Y. Du, D. Wang, Q. Xie, and S. Xie, "Pathways of mesoscale variability in the South China Sea," *Chin. J. Oceanol. Limnol.*, vol. 28, pp. 1055–1067, 2010.

[26] W. T. Liu and X. Xie, "Spacebased observations of the seasonal changes of South Asian monsoons and oceanic responses," *Geophys. Res. Lett.*, vol. 26, no. 10, pp. 1473–1476, 1999.

[27] E. C. J. Oliver, "Intraseasonal variability of sea level and circulation in the Gulf of Thailand: The role of the Madden–Julian Oscillation," *Climate Dyn.*, vol. 42, pp. 401–416, 2014.

[28] D. Wang, W. Wang, P. Shi, P. Guo, and Z. Gan, "Establishment and adjustment of monsoon-driven circulation in the South China Sea," *Sci. China, Ser. D Earth Sci.*, vol. 46, no. 2, pp. 173–181, 2003.

[29] S. Cai, X. Long, R. Wu, and S. Wang, "Geographical and monthly variability of the first baroclinic Rossby radius of deformation in the South China Sea," *J. Mar. Syst.*, vol. 74, nos. 1/2, pp. 711–720, 2008.

[30] G. R. North, T. L. Bell, R. F. Cahalan, and F. J. Moeng, "Sampling errors in the estimation of empirical orthogonal functions," *Monthly Weather Rev.*, vol. 110, no. 7, pp. 699–706, 1982.

[31] Y. Du, D. Wu, F. Liang, J. Yi, Y. Mo, Z. He, and T. Pei, "Major migration corridors of mesoscale ocean eddies in the South China Sea from 1992 to 2012," *J. Mar. Syst.*, vol. 158, pp. 173–181, 2016.

[32] G. Chen, Y. Hou, and X. Chu, "Mesoscale eddies in the South China Sea: Mean properties, spatiotemporal variability, and impact on thermohaline structure," *J. Geophys. Res.*, vol. 116, 2011, Art. no. C06018.

[33] J. L. Wilkin, and W. G. Zhang, "Modes of mesoscale sea surface height and temperature variability in the East Australian current," *J. Geophys. Res.*, vol. 112, 2007, Art. no. C01013.

[34] J. Hu, Q. Zheng, Z. Sun, and C.-K. Tai, "Penetration of nonlinear Rossby eddies into South China Sea evidenced by cruise data," *J. Geophys. Res.*, vol. 117, 2012, Art. no. C03010.

[35] D. Wang, Q. Liu, Q. Xie, Z. He, W. Zhuang, Y. Shu, X. Xiao, B. Hong, X. Wu, and D. Sui, "Progress of regional oceanography study associated with western boundary current in the South China Sea," *Chin. Sci. Bull.*, vol. 58, no. 11, pp. 1205–1215, 2013.

Kewei Lyu received the Ph.D. degree in physical oceanography from Xiamen University, Xiamen, China, in 2015.

He is currently a Postdoctoral Researcher with the University of California, Irvine, CA, USA. His research interests include sea-level variability and change, regional oceanography of the South China Sea, and applications of ocean remote sensing products.
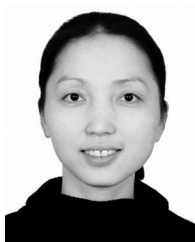
Xiao-Yi Yang received the Ph.D. degree in physical oceanography from the South China Sea Institute of Oceanology, Chinese Academy of Sciences, Guangzhou, China, in 2007.

From 2008 to 2010, she was a Postdoctoral Researcher with the Canadian Centre for Climate Modelling and Analysis. Since 2010, she has been an Associate Professor with Xiamen University, Xiamen, China. Her research interests include large-scale ocean-atmosphere interaction and global climate change.

Dongxiao Wang received the Ph.D. degree in physical oceanography from the Ocean University of Qingdao, Qingdao, China, in 1996.

He is currently a Professor with the South China Sea Institute of Oceanology, Chinese Academy of Sciences, Guangzhou, China, where he is also a Vice-director. His research interests include the air–sea interaction and ocean dynamics in the South China Sea and Indian Ocean.

Dr. Wang is the Member of the American Geophysical Union, the American Meteorological Society, and the Asian Oceania Geosciences Society.

Quanan Zheng received the Ph.D. degree in physical oceanography from the Institute of Oceanology, Chinese Academy of Sciences, Qingdao, China, in 1987.

He is currently a Senior Research Scientist with the University of Maryland, College Park, MD, USA. His research interests include ocean remote sensing, ocean surface processes, upper ocean dynamics, mesoscale ocean dynamics, and solitary waves in the atmosphere and ocean.

Jianyu Hu received the Ph.D. degree in physical oceanography from Tohoku University, Sendai, Japan, in 2001, and the Ph.D. degree in environmental science from Xiamen University, Xiamen, China, in 2002.

He is currently a Professor with Xiamen University, Xiamen, China. His research interests include physical oceanography and regional environmental oceanography, focusing on the study of ocean circulation, upwelling, ocean fronts, and tides.